Mon. Not. R. Astron. Soc. **373,** 1379–1388 (2006) doi:10.1111/j.1365-2966.2006.11164.x

Cloud dispersal in turbulent flows

F. Heitsch,[1,2★] A. D. Slyz,[3] J. E. G. Devriendt[3] and A. Burkert[2]

[1]*Department of Astronomy, University of Michigan, 500 Church Street, Ann Arbor, MI 48109-1042, USA*
[2]*University Observatory Munich, Scheinerstr. 1, 81679 Munich, Germany*
[3]*Université de Lyon 1, Centre de Recherche Astronomique de Lyon, Observatoire de Lyon, 9 Avenue Charles André, F-69230 Saint-Genis Laval, France; CNRS, UMR 5574, Ecole Normale Supérieure de Lyon*

Accepted 2006 September 26. Received 2006 September 21; in original form 2006 April 23

ABSTRACT

Cold clouds embedded in warm media are very common objects in astrophysics. Their disruption time-scale depends strongly on the dynamical configuration. We discuss the evolution of an initially homogeneous cold cloud embedded in warm turbulent gas. Within a couple of dynamical time-scales, the filling factor of the cold gas within the original cloud radius drops below 50 per cent. Turbulent diffusivities estimated from the time evolution of radial filling factor profiles are not constant with time. Cold and warm gas are bodily transported by turbulence and mixed. This is only mildly indicated by column density maps. The radiation field within the cloud, however, increases by several orders of magnitudes due to the mixing, with possible consequences for cloud chemistry and evolution within a few dynamical time-scales.

Key words: hydrodynamics – radiative transfer – turbulence – ISM: clouds – ISM: kinematics and dynamics.

1 MOTIVATION

Molecular clouds (MCs) in the Galaxy exhibit a wealth of structures in (column) densities, velocities and magnetic fields. The observed structural properties strongly suggest that MCs are highly dynamical objects within a turbulent interstellar medium (ISM). Especially, the observed non-thermal linewidths (Falgarone & Philips 1990; Williams, Blitz & McKee 2000) indicate the turbulent nature of the clouds. The importance of MC turbulence for the process of star formation has been the subject of many investigations (see Elmegreen & Scalo 2004; Mac Low & Klessen 2004, for overviews).

Turbulent mixing is an ever-recurring theme in the ISM. Classical turbulent mixing accelerates diffusive transport by a factor of the order of the Reynolds number of the flow (e.g. Schatzman 1977). de Avillez & Mac Low (2002, 2003) and Klessen & Lin (2003) discussed the applicability of turbulent transport and mixing to a turbulent ISM, stating that transport rates can vary strongly with time, sometimes exhibiting superdiffusive behaviour due to bulk motions of the gas. Turbulent mixing has also been held responsible as a source of the highly ionized gas observed around high-velocity clouds in the Galactic halo (e.g. Fox et al. 2004), although it is unclear whether turbulent mixing or evaporation by heat conduction is the dominating process (Cowie & McKee 1977; McKee & Cowie 1977; Balbus & McKee 1982; Lazarian 2006).

A spherical cold cloud travelling through a warm uniform medium dissolves approximately within a time-scale $\tau_{\rm d} = M_{\rm cl}/(\rho\ \pi R_{\rm cl}^2\ v)$, where $M_{\rm cl}$ is the cloud's initial mass, ρ its density, $R_{\rm cl}$ its radius, and v its velocity (Nulsen 1982). The main agent is the Kelvin–Helmholtz instability, whose efficiency in dissolving the cloud depends on the cloud's physical properties, for example, whether it is self-gravitating (Murray et al. 1993) – in which case there exists a critical mass above which the cloud remains stable – or whether it suffers radiative energy losses (Vietri, Ferrara & Miniati 1997) – in which case the instability can be damped, stabilizing the cloud.

Cloud dispersal by hydrodynamical instabilities might be of considerable importance: observations and theoretical considerations suggest that MCs in the solar neighbourhood have lifetimes of approximately 2–3 Myr, which would necessitate close to instantaneous star formation once the clouds have formed (Elmegreen 1993, 2000; Hartmann, Ballesteros-Paredes & Bergin 2001; Pringle, Allen & Lubow 2001; Hartmann 2003). While stellar feedback in the form of supernovae could disrupt a cloud, low-mass stars in solar neighbourhood clouds might not be efficient enough to achieve such a rapid dispersal (e.g. Mac Low 2004). An alternative route has been offered by interpreting MCs as transient objects generated by large-scale colliding flows (Ballesteros-Paredes, Hartmann & Vázquez-Semadeni 1999; Hartmann, Ballesteros-Paredes & Bergin 2001; Heitsch et al. 2005, 2006; Vázquez-Semadeni et al. 2006). In this picture, the flows in which the clouds form eventually might lead to their dispersal within a few Myr.

We investigate the role of turbulence for the overall evolution of a cold cloud – corresponding to the cold neutral medium – embedded in warm gas whose parameters are representative of the warm ionized medium. Specifically, we are interested in the time-scales on which a cold solid cloud will disperse in a turbulent environment, and in the evolution of the radiation field within the cloud (Section 2). A detailed, time-independent study of the radiation

★E-mail: fheitsch@umich.edu

field in a filamentary cloud can be found in Bethell et al. (2004) and Bethell, Zweibel & Li (2006).

We find (Section 3) that the warm and cold components are efficiently mixed by bodily transport. However, the central optical depth stays comfortably above 1 even for late times. At first, this might seem contradictory, however, the local radiation field within the cloud increases by several orders of magnitude within a couple of dynamical times. Turbulent diffusivities derived from the expansion of the cold cloud generally are not constant with time. Possible consequences for cloud lifetimes and evolution are discussed in Section 4.

2 THE PROBLEM AND ITS SET-UP

We start with a uniform sphere of cold dense gas in a warm diffuse ambient medium. The system is initially completely in thermal and almost in turbulent pressure[1] equilibrium. One model set (sequence A) is purely adiabatic, that is, the two-phase structure of the system will get erased with time as gas with temperature intermediate to the two initial temperatures is created. The second set (sequence C) keeps the identities of the warm and cold phases distinct by a combination of heating and cooling processes (Wolfire et al. 1995) typical for the warm and cold atomic ISM. Thus, we study turbulent mixing under conditions with and without radiative losses. Initially, both gas components are in thermal equilibrium at temperatures that for the radiative case correspond to the two stable temperature regimes, that is, there is no gas in the thermally unstable regime initially. The lower initial temperature is set to $T = 31$ K, and the density contrast between warm and cold gas is 300, with $n_0 = 0.5\,\mathrm{cm}^{-3}$ in the warm phase at $T = 9.2 \times 10^3$ K. The cubic box is periodic in all directions, with a side length, L, of 44 pc, and the cold gas sphere starts out with a radius of 4.4 pc.

Instead of studying the cloud evolution within a shear flow, we resort to a more direct way of treating turbulence, namely by initially imposing a velocity field drawn from a random Gaussian distribution (see e.g. Mac Low et al. 1998). Power is allotted in Fourier space only to the largest scales, and with random phases. This is meant to mimic the effect of turbulence generated by an unspecified source on larger scales. The initial Mach number in the warm gas $\mathcal{M}_0 = 2$ or 3 – corresponding to $v_0 = 22.4\ \mathrm{km\,s^{-1}}$ and $v_0 = 33.6\ \mathrm{km\,s^{-1}}$ – is higher than Mach numbers commonly ascribed to the warm ISM, however, since the turbulence is not driven, the system acquires reasonable values of $\mathcal{M}$ once turbulence is fully developed. The justification for this will be discussed in Section 3.4. One might argue that the scenario of a uniform, spherical cold cloud evolving in a decaying turbulent velocity field is only of limited physical relevance, since the Galactic ISM turbulence is to a large extent thought to be driven by supernovae (Cox & Smith 1974; McKee & Ostriker 1977; Rosen & Bregman 1995; de Avillez 2000; de Avillez & Berry 2001). However, the goal of this study is not to model the evolution of a cold (possibly molecular) cloud, but to demonstrate that even under unfavourable conditions (decaying turbulence, no stellar feedback, no gravitational fragmentation, starting with a uniform spherical cloud), cold clouds fragment and disperse sufficiently within a dynamical time-scale so that the internal structure of the cloud is thoroughly altered. Driven turbulence and/or stellar feedback obviously would lead to faster dispersal, while gravitational fragmentation would result in a smaller gas filling factor, thus opening holes and channels for radiation and energy (possibly in form of waves, see e.g. Hennebelle & Inutsuka 2006) to enter the cloud. For this reason also a non-uniform cloud would be more prone to disperse in a turbulent environment.

The adiabatic model sequence we will denote by A, the radiatively cooled model by C. The initial Mach number of the model is denoted by '2' or '3', for Mach 2 or 3. We ran models at linear resolutions of 128^3 and 256^3 cells, indicated by the letters a and b, respectively. The choice of the – rather small – initial cloud radius could raise concerns about how well even the 256^3 models are resolved. Thus, we ran an additional model, A2l, with the same parameters as the adiabatic model at Mach 2, A2b, except for the initial cloud radius, here set to 8.8 pc.

Initially, the system is in thermal and near turbulent pressure balance, that is, for turbulent pressure balance

$$\langle v^2 \rangle_\mathrm{c} = \frac{\rho_\mathrm{w}}{\rho_\mathrm{c}} \langle v^2 \rangle_\mathrm{w} \tag{1}$$

holds, with velocities v and densities ρ. The indices stand for the cold and warm phase. The near pressure balance reduces motions due to pressure differences and therefore allows us to make more valid statements about turbulent transport or mixing in this idealized set-up.

The numerical scheme is based on the 2nd order Bhatnagar–Gross–Krook formalism (Prendergast & Xu 1993; Slyz & Prendergast 1999; Heitsch et al. 2004; Slyz et al. 2005), allowing control of viscosity and heat conduction. The code evolves the Navier–Stokes equations in their conservative form to second order in time and space. The hydrodynamical quantities are updated in time-unsplit form.

We employed the same heating and cooling prescriptions as Heitsch et al. (2005, 2006), based on Wolfire et al. (1995). The same caveats apply, especially that we are discussing the mixing between the warm and cold ISM, and that we are not including molecular gas. Thus, while the parameters of our cold cloud are consistent with values for 'giant MCs', we neglect the effects of molecular line cooling and chemistry.

The code is equipped with Lagrangian tracer particles that are initially deployed within the cold cloud at a resolution of one particle per grid cell. The particles are advected with the gas flow, so that they allow us to study the history of the cold gas.

We restricted the models to hydrodynamics with heating and cooling, leaving out gravity and magnetic fields. Depending on their strength, fields could suppress shear instabilities, while gravity might lead to more compact dense structures and fragmentation. This could have a twofold effect, as will be discussed in Section 4.

3 RESULTS

3.1 Morphologies

A first impression of the efficiency of turbulent mixing can be gleaned from a time sequence of column density maps (Fig. 1). Column densities are integrated along the z-axis and shown at times $t = \tau_\mathrm{e}$, $t = 3\tau_\mathrm{e}$ and $t = 5\tau_\mathrm{e}$, where $\tau_\mathrm{e} = L/v_0 \approx 2$ Myr, a nominal turbulent flow crossing time in terms of the total box length and the rms velocity in the warm diffuse gas. Despite the fact that we are

[1] As discussed by, for example, Ballesteros-Paredes (2006), the concept of turbulent pressure is only applicable if there exists a scale separation between the (large) object scale and the (small) turbulent scale. In a medium without scale separation – e.g. with a self-similar turbulent power spectrum – the term 'turbulent pressure' should be read as 'turbulent kinetic energy density'. It is in this sense we will use the term 'turbulent pressure' throughout the paper.

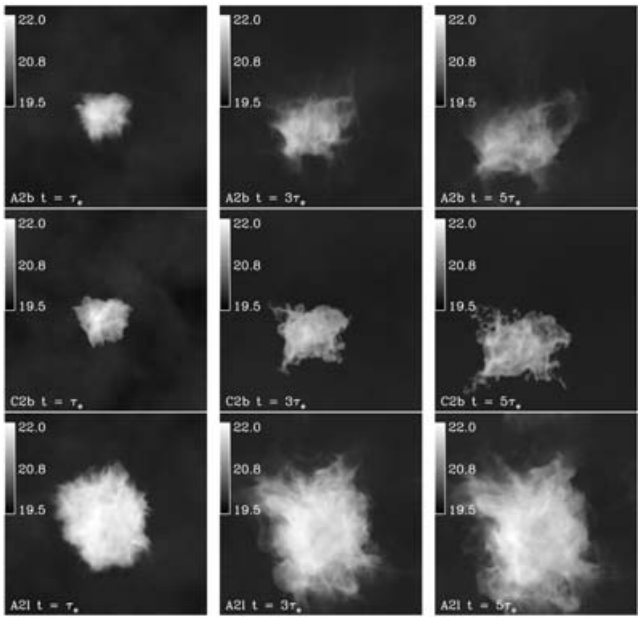

Figure 1. Column density maps of model A2b (top), C2b (centre), and A2l (bottom) projected along the z-axis, for times $t = \tau_e$, $3\tau_e$ and $5\tau_e$, where $\tau_e \approx 2$ Myr is the initial turbulent crossing time. Grey-scale corresponds to log $N(\mathrm{cm}^{-2})$.

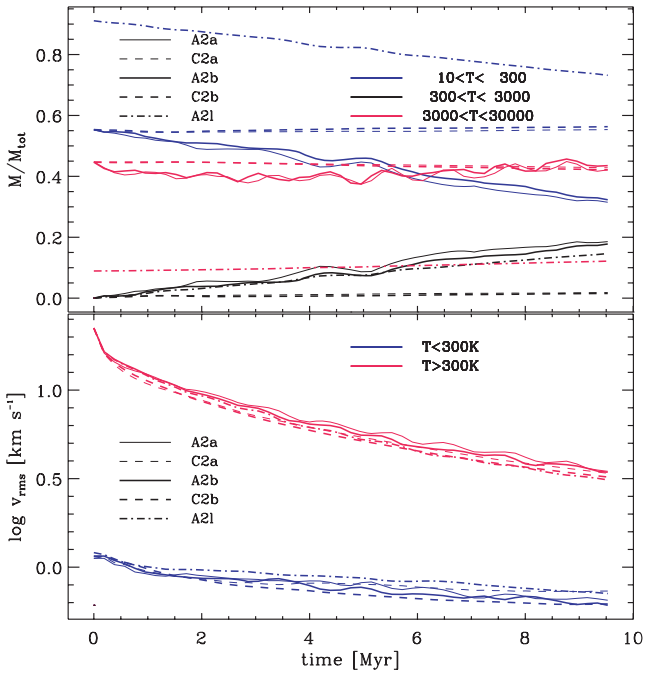

Figure 2. Top: Mass fraction over the whole simulation volume for the three thermal regimes indicated, against time, for models A2a/b and C2a/b at resolutions $N = 128^3$ and 256^3, and for model A2l (at $N = 256^3$). Bottom: rms velocity $\langle v^2 \rangle^{1/2}$ for cold and warm gas against time, for the same models and resolutions. Note that red and blue lines here denote $T > 300$ K and $T < 300$ K, respectively.

looking at column densities here, the overall effect of the cloud's turbulent dispersal is clearly visible.

The most noticeable difference between the adiabatic models A2b and A2l (top and bottom) on the one hand and the radiative models (C2b, centre) on the other is that for the latter, the transition between low and high column densities is much more marked, that is, the column density maps appear (especially in the later stages) less 'frothy'. As we will see below, this is a direct consequence of the cooling.

In overall appearance, for both the adiabatic and radiative models the cloud stays more or less compact, although fingers of cold, dense material are clearly sprouting from the core.

3.2 Mass fractions and Dynamics of the Warm and Cold Gas

Since we will be discussing the turbulent mixing of the warm and cold gas, first, we need to understand the dynamics and evolution of each of the phases. Note that – strictly speaking – the concept of 'phases' can be misleading not only for the adiabatic case, but also for the thermally bistable case, because of the importance of dynamics (see e.g. Vázquez-Semadeni, Gazol & Scalo 2000; Heitsch et al. 2006; Vázquez-Semadeni et al. 2006). Motivated by the bistable models (sequence C), we split the model-ISM into three regimes, namely a cold phase with temperatures $T < 300$ K, a warm phase ($T > 3000$ K) and an intermediate phase with $300 < T < 3000$ K. The corresponding mass fractions (Fig. 2, top panel) evolve quite differently for adiabatic and radiative models. The mass fractions are taken over the whole simulation volume. Since the cloud in model A2l has an initial radius twice as large as in the other models, it starts off with a larger cold mass fraction and a smaller warm mass fraction. The intermediate temperature regime evolves similarly to that in models A2a/b.

In the adiabatic case (A2a/b/l), some of the cold gas is lost to the intermediate regime, while the mass fraction in the warm phase stays pretty much constant. In contrast, the radiative case (C2a/b) keeps constant mass fractions in each of the three temperature regimes over the whole simulation time (i.e. 5 dynamical times). Heating and cooling time-scales are much shorter than the dynamical time-scales, so that gas cannot collect in the intermediate regime, which for model C2a/b corresponds to the thermally unstable regime. In particular, in C2a/b gas which is heated by (viscous) shear at the cloud boundaries 'falls back' to its previous (cold) thermal state, while for A2a/b, this gas has no way to return to its previous temperature except by adiabatic cooling. Varying the resolution does not change the mass fractions appreciably. Model C2a/b displays a tiny increase of the cold mass fraction. This stems from the compression of warm gas when it collides with the cold cloud rim. Once the warm gas' density increases, cooling sets in, and this compressed gas is added to the cold gas component. However, as Fig. 2 shows, this effect is negligible.

In contrast to the evolution of the mass fractions differing for the adiabatic and radiative models, the rms velocities of the gas in the cold and warm temperature regimes evolve similarly for both sets of models. Fig. 2 (bottom panel) mirrors the initial pressure balance (equation 1): velocities in the cold phase start out lower by a factor of approximately 17. For each of the models A and C, the velocities in the cold and warm phase decay, albeit at different rates. Resolution effects do not affect the decay (the thin and thick lines are nearly indistinguishable). Comparing model A to C, the radiative losses occurring in C do not lead to significantly different decay rates. Radiative losses would become important in regions of high compression, however, the turbulence initially decays quickly below Mach 1 in both the warm and cold gas, limiting the compression. We discuss the time evolution of the cold and warm pressure profiles in

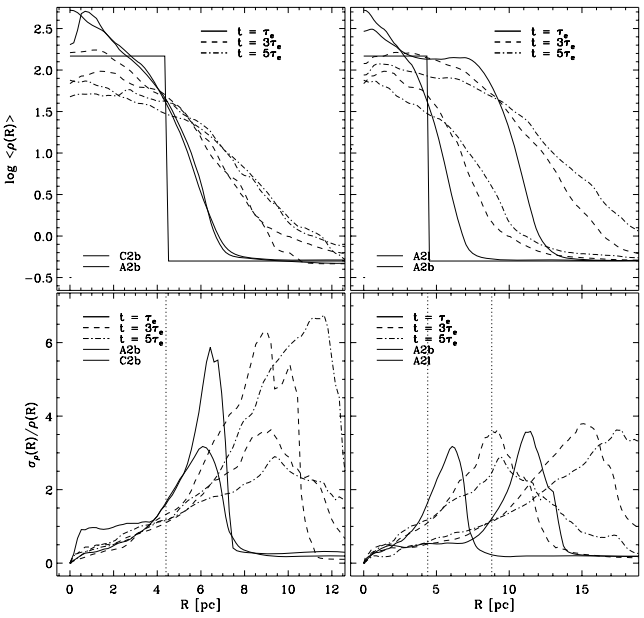

Figure 3. Top: Radial density profiles for models A2b, C2b and A2l, at the times indicated. Model A2b is shown in thick lines in both plots. The thin solid step function gives the initial density profile for models A2b and C2b. The initial density profile of model A2l extends out to 8.8 pc. Bottom: Relative s.d. of density profile (equation 3). The dotted vertical line denotes the initial radius.

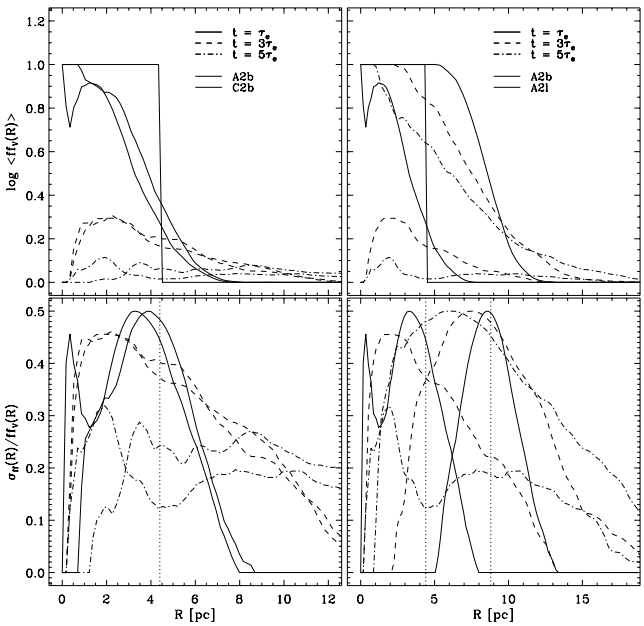

Figure 4. Top: Radial cold gas filling factor profile for models A2b, C2b and A2l at the times indicated. Model A2b is shown in thick lines in both plots. The thin solid step function gives the initial cold gas filling factor profile for models A2b and C2b. The initial profile of model A2l extends out to 8.8 pc. Bottom: Relative s.d. of filling factor profile (analogous to equation 3). The dotted vertical line denotes the initial radius.

detail in Section 3.3. The larger cloud (model A2l) shows the same velocity decay as its small counterparts.

3.3 Radial profiles

Does the cloud break up in the turbulent environment, and if so, how quickly does this happen? The answer depends strongly on the quantity we are looking at. Since we are interested in an average measure of the cloud's structure, we take averages over shells and discuss the resulting radial profiles. The shell centres coincide with the instantaneous centre of mass of the cloud (the cloud itself moves a little in the background flow). We begin with the density profiles (Fig. 3).

Clearly, the turbulent motions lead to a spreading-out of the cloud, mirrored in the density-weighted average radius

$$\langle R\rangle_M \equiv \frac{\int_0^R r\,\rho(r)\,\mathrm{d}r}{\int_0^R \rho(r)\,\mathrm{d}r} \tag{2}$$

of the cloud, which roughly doubles within $5\tau_\mathrm{e} = 10$ Myr. As Fig. 1 already indicates, the radial density profiles show a substantial variation at fixed radius R (Fig. 3, lower panel), up to six times the actual density value. The quantity

$$\frac{\sigma_\rho(R)}{\rho(R)} \equiv \frac{\langle(\rho(R)-\langle\rho\rangle)^2\rangle^{1/2}}{\rho(R)} \tag{3}$$

plotted is the relative s.d. on the mean density over a sphere at radius R. The strongest variations are expected at the cloud rim, which travels (upper panel) outwards, so that the peak of the density variations is seen at larger radii for later times. Already after one dynamical time, the cloud is far from being a solid sphere.

A more stringent measure is the radial volume filling factor profile for gas in the cold phase (Fig. 4). Volume filling factors are measured on shells at given R. As in Section 3.2, the temperature threshold to distinguish between the warm and cold phase is set at $T = 300$ K. The step function in the upper panel gives the initial condition, which of course shows a cold gas filling factor of 1 for $R \leqslant 4.4$ pc (or $R \leqslant 8.8$ pc for model A2l).

The first obvious difference between the radiative and adiabatic case is that the adiabatic case seems to mix faster the cold and warm phase at more radii. However, this is not that surprising, since for the adiabatic case *any* gas with $T > 300$ K is lost for the cold gas filling factor, while for the radiative case, gas which has left the cold phase can only be found in the warm phase (there is no intermediate-phase gas, Fig. 2, top panel) but because of the short cooling times, this gas can quickly return to the cold phase. In other words the filling factor gives an unambiguous measure of the degree of mixing between cold and warm gas only for the thermally bistable, radiative case (C2b), since there is (close to) zero conversion between the gas phases (see also discussion on tracer particles below).

After 2 Myr (corresponding to $t = \tau_\mathrm{e}$), the volume filling factor of the cold gas measures 40 per cent for the radiative case, and ∼25 per cent for the adiabatic case at the initial cloud boundary, that is, more than half of the volume is occupied by warm gas. Note that especially in the radiative case, the *mass fractions* of cold and warm gas stay constant, that is, cold and warm gas are bodily transported. This can be gleaned from Fig. 5. It shows the histogram of the fraction of Lagrangian tracer particles $N_\mathrm{P}(T < 300\ \mathrm{K})/N_\mathrm{P}$ within the cloud that stay at temperatures $T < 300$ K for a time interval Δt. If there were no turbulence in the models, all the particles would stay at $T < 300$ K for the whole duration of the simulation, that is, we would have $N_\mathrm{P}(T < 300\ \mathrm{K})/N_\mathrm{P} = 1$ at $\Delta t = 10$.

Most of the particles stay cold for longer than 9 Myr, that is, for the simulation's time extent. In other words, the constancy of the mass fractions in Fig. 2 indeed results only to a very minor extent from the conversion of cold to warm gas and vice versa: mass in the cold and warm regime is separately conserved. This is less valid for

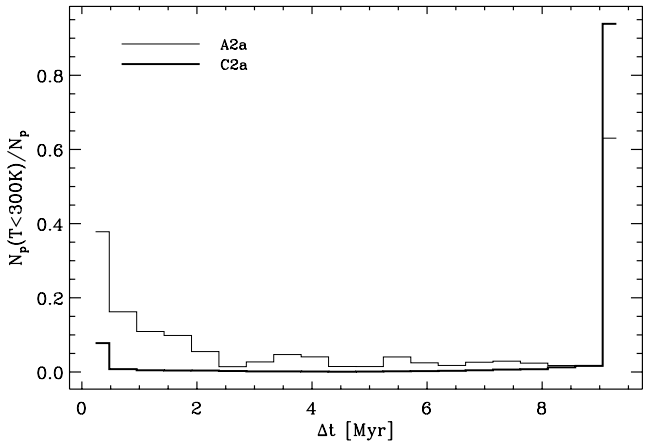

Figure 5. Histogram of fraction of tracer particles in the flow staying at $T <$ 300 K for a time interval Δt. Most tracer particles stay cold over the whole simulation time ($\Delta t > 9$ Myr) for model C2b (thick line), while for model A2b (thin line), only ∼60 per cent of the particles stay at $T < 300$ K.

the adiabatic case, which obviously loses some of its cold material. But still, the bulk of the initially cold gas stays cold for the whole simulation time.

Besides turbulent transport, an overpressure in the cold cloud could lead to 'expansion'. So far, our diagnostics cannot distinguish between these two mechanisms for cloud expansion. Fig. 6 shows the radial profiles of the pressures for models A2b, C2b and A2l. The total pressure $P_{\rm tot}$ has been split into the thermal pressure P, and the turbulent pressure $P_{\rm trb}$, from which we have removed the contribution of the translational velocity $\langle v \rangle$, as

$$P_{\rm tot} = P + \rho(v - \langle v \rangle)^2, \tag{4}$$

where the average extends over coherent cold and warm regions. The top row gives the radial pressure profile for gas with $T > 300$ K, and the bottom row shows the profile for gas with $T < 300$ K. The time sequence reveals the mixing of the warm and cold component, since $P(T > 300$ K) can be defined at smaller radii for later times, while $P(T < 300$ K) spreads outward to large radii resulting in warm and cold gas co-existing at an increasingly larger radial range. For $t = 0$, models A2b and C2b are of course identical. The thermal pressure is constant, while the turbulent pressure (and thus the total pressure) is slightly lower within the cold cloud than in the warm medium. This serves as a safeguard against initially overpressuring the cloud by turbulent pressure. At $t = \tau_{\rm e}$ (centre column), the cold dense material (i.e. the cloud) in both models is overpressured relative to the warm gas. This comes mostly from an overshoot in the density, since turbulent pressure and thermal pressure have (approximately) the same radial dependence: the cloud is initially slightly compressed by the higher turbulence in the warm medium (see also the radial density profiles, Fig. 3). In Fig. 2 (bottom panel) we saw that the rms velocity – and because of the close to constant density in the respective phases, the kinetic energy – decays faster for the warm gas than for the cold gas. Both effects together lead to the overpressure in the cold gas at $t = \tau_{\rm e}$. At later times, this pressure imbalance has cancelled out, and the warm and cold phases are mixed. There is still a turbulent pressure excess at small radii, however, the turbulence has decayed so far that its dynamical effects are insignificant.

For the adiabatic run, at $t = \tau_{\rm e}$ the thermal pressure has risen from its initial value both for the cold and warm gas. The turbulent pressure on the other hand, has dropped by about a factor of 3 for the warm gas, but not as much for the cold gas, suggesting that

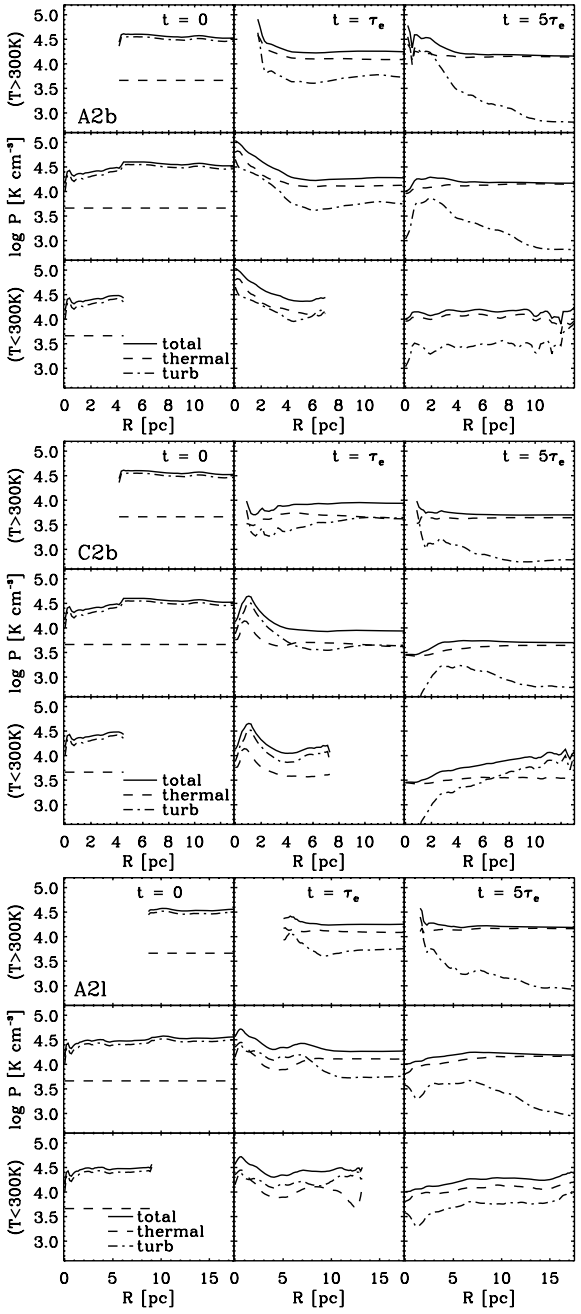

Figure 6. Radial pressure profiles for models A2b (top), C2b (centre) and A2l (bottom) for times 0, $\tau_{\rm e}$ and $5\tau_{\rm e}$. In each panel, from top to bottom: radial pressure profile for gas at $T > 300$ K, total radial pressure profile, and radial pressure profile for gas at $T < 300$ K. Plotted are the total pressure (solid lines), the thermal pressure (dashed) and the turbulent pressure (see text, dash–dotted line). The three columns per model denote the measurement times $t = 0$, $t = \tau_{\rm e}$ and $t = 5\tau_{\rm e}$.

turbulent energy in the warm phase has been used to heat the warm phase and to drive the turbulence in the cold phase, since the thermal energy in the cold phase increased and the turbulent energy remains unchanged. With the total energy conserved, some of the energy in the cold gas has to come from the warm gas. For the radiative model at $t = \tau_{\rm e}$ the transfer of energy from the warm to the cold gas is less marked but seems to have occurred nevertheless. The cold gas thermal and turbulent pressure in the innermost radii increase

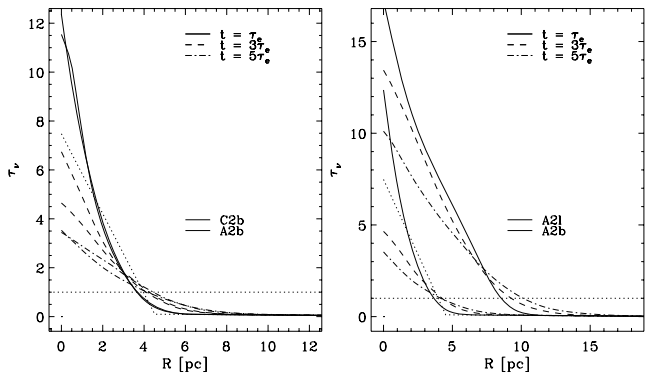

Figure 7. Left-hand panel: Radial optical depth profile for models C2b (thin lines) and A2b (thick lines), at the times as indicated in the plot. The thick dotted line gives the initial optical depth profile, while the thin dotted line denotes $\tau_\nu = 1$. Right-hand panel: Same plot for models A2l (thin lines) and A2b (thick lines). Note that the optical depth range is larger for model A2l.

from their initial values. The thermal pressure of the warm gas on the other hand has hardly changed from its initial value even though the turbulent pressure has dropped by almost an order of magnitude from its initial value at all radii where warm gas exists. Again, the thermal and/or turbulent pressure increase in the cold gas has to come from the warm gas. Model A2l shows essentially the same behaviour as model A2b.

The radial density profile allows us to determine the average optical depth at a given radius (Fig. 7). To arrive at meaningful optical depths, we scaled the effective absorption coefficient α_ν such that the central optical depth is initially arbitrarily set to $\tau_c = 7.5$ for models A2a/b and C2a/b, and to $\tau_c = 15$ for model A2l. This corresponds to an absorption coefficient of $\alpha_\nu = 3.6 \times 10^{-21}$ cm^2. For comparison, Spitzer (1978) gives an effective combined cross-section for absorption and scattering on grains of $\alpha_\nu = 1.2 \times 10^{-21}$ cm^2 at a wavelength of 100 nm. Likewise, we do not take into account the effect of scattered light.

There are no marked differences between the adiabatic and the radiative case. This as well as the fact that $R(\tau = 1)$ does not change appreciably over time is a direct consequence of the radial density profiles (Fig. 3). At $t = \tau_e$, the optical depth in the centre has increased due to an initial compression, just to drop at later times because of turbulent dispersal. This 'overshoot' is mirrored in the density profiles (Fig. 3, top panel).

The central optical depth τ_c drops by approximately a factor of 2, but does not fall below $\tau = 1$. That τ_c changes at all with time might come as a surprise, but is a consequence of the exchange of dense and diffuse material at approximate pressure equilibrium: the filling factor of dense material on a spherical surface at fixed radius decreases, lowering the central optical depth.

3.4 Turbulent diffusivity

The evolving radial density and filling factor profiles (Figs 3 and 4) suggest to estimate the (turbulent) diffusivity by fitting them to the expected profiles resulting from the time evolution of a step function under the effect of diffusion. An (inert) quantity q in a turbulent environment obeys the advection-diffusion equation

$$(\partial_t + \boldsymbol{u} \cdot \nabla) q = \lambda \nabla^2 q, \tag{5}$$

where $\boldsymbol{u}$ is the velocity, and λ the microscopic diffusivity, which has been assumed to be independent of location and direction. Equation (5) can be rewritten (see e.g. appendix in Heitsch et al. 2004) as

$$\partial_t \langle q \rangle = (\lambda_e + \lambda) \nabla^2 \langle q \rangle, \tag{6}$$

under the – contestable – assumption of a separation between the small-scale turbulent velocity field and the large-scale variations in the quantity $\langle q \rangle$, where the averages have removed variations due to the small-scale turbulence. The 'turbulent diffusivity' $\lambda_e \equiv u_{\rm rms} L$ is the product of the rms velocity and the characteristic length-scale over which a gas parcel maintains $u_{\rm rms}$ (see e.g. Landau & Lifshitz 1966). In the ISM, the Reynolds number $Re \equiv \lambda_e / \lambda \gg 1$, generally, so that λ can be neglected for turbulent transport studies. Quasi-linear diffusion theory (see e.g. Moffatt 1978) holds that λ_e can be regarded as constant.

Since our model clouds start out with a uniform density, we can follow the discussion by de Avillez & Mac Low (2002) and study the turbulent diffusive evolution of a step function profile. A one-dimensional density distribution evolves as

$$n(x,t) = \frac{1}{2\sqrt{\pi \lambda_e t}} \int_{-\infty}^{\infty} n(x', t=0)\, \mathrm{e}^{-(x-x')^2/4\lambda_e t}\, \mathrm{d}x' \tag{7}$$

under diffusion. The initial conditions can be written as $n(x \leqslant R_0,\ t = 0) = n_1$ and $n(x > R_0,\ t = 0) = n_0$, where R_0 is the initial cloud radius at $t = 0$. Then, the density distribution at time t is given by

$$n(x,t) = n_0 + \frac{n_1 - n_0}{2} \left[1 - \mathrm{erf}\left(\frac{1}{2} \frac{x - R_0}{\sqrt{\lambda_e t}} \right) \right], \tag{8}$$

where erf(x) is the error function. A similar expression is valid for the filling factor $f(x,t)$, if we replace $n(x,t)$ by $f(x,t)$, and set $n_0 = 0$ and $n_1 = 1$. Since the initial radius R_0 is known, we can fit equation (8) to the available density and filling factor profiles at given times t, and thus determine the diffusivity λ_e by a one-parameter Levenberg–Marquardt least-squares minimization (e.g. Press et al. 1992) for each available time-step of a model.

Fig. 8 shows the resulting diffusivities for the filling factor profiles (top left-hand panel) and the density profiles (top right-hand panel) for all models. The centre row gives the 1σ errors of the profile fits, and the bottom row contains the reduced $\chi^2_{\rm red}$ for the filling factor profiles (bottom left-hand panel) and for the density profiles (bottom right-hand panel). Reliable fits we select (somewhat arbitrarily) by $\chi^2_{\rm red} < 2$, agreeing well with a selection by eye.

Clearly, the filling factor profiles lead to much better fits than the density profiles. Figs 3 and 4 explain this: the filling factor cannot rise above 1 or drop below 0, thus constraining the profiles for the least-squares minimization, while the density profiles actually increase above n_1 and drop below n_0 because of travelling waves. Moreover, in deriving equation (8), we assumed that $n(x \leqslant R_0,\ t = 0) = n_1$ is valid for all $x < R_0$, and not only for $0 \leqslant x \leqslant R_0$, as by construction of the initial conditions. This assumption is certainly not valid any more at later times.

We first notice that the diffusivities determined by least-squares fitting (symbols in top row of Fig. 8) are not constant with time. Until $\sim$3 Myr they all increase. The increase however is less than an order of magnitude. The filling factor profiles return slightly decreasing diffusivities for later times and for all models except model A2l. de Avillez & Mac Low (2002) found that the diffusivities increase exponentially with time. Since they start with an unperturbed medium and then drive the turbulence via supernova explosions, the growing diffusivities could be a result of the increasing rms velocity. In our models, a similar effect is causing the initial rise of λ_e. The turbulent diffusivity increases while the turbulent cascade is building up. At

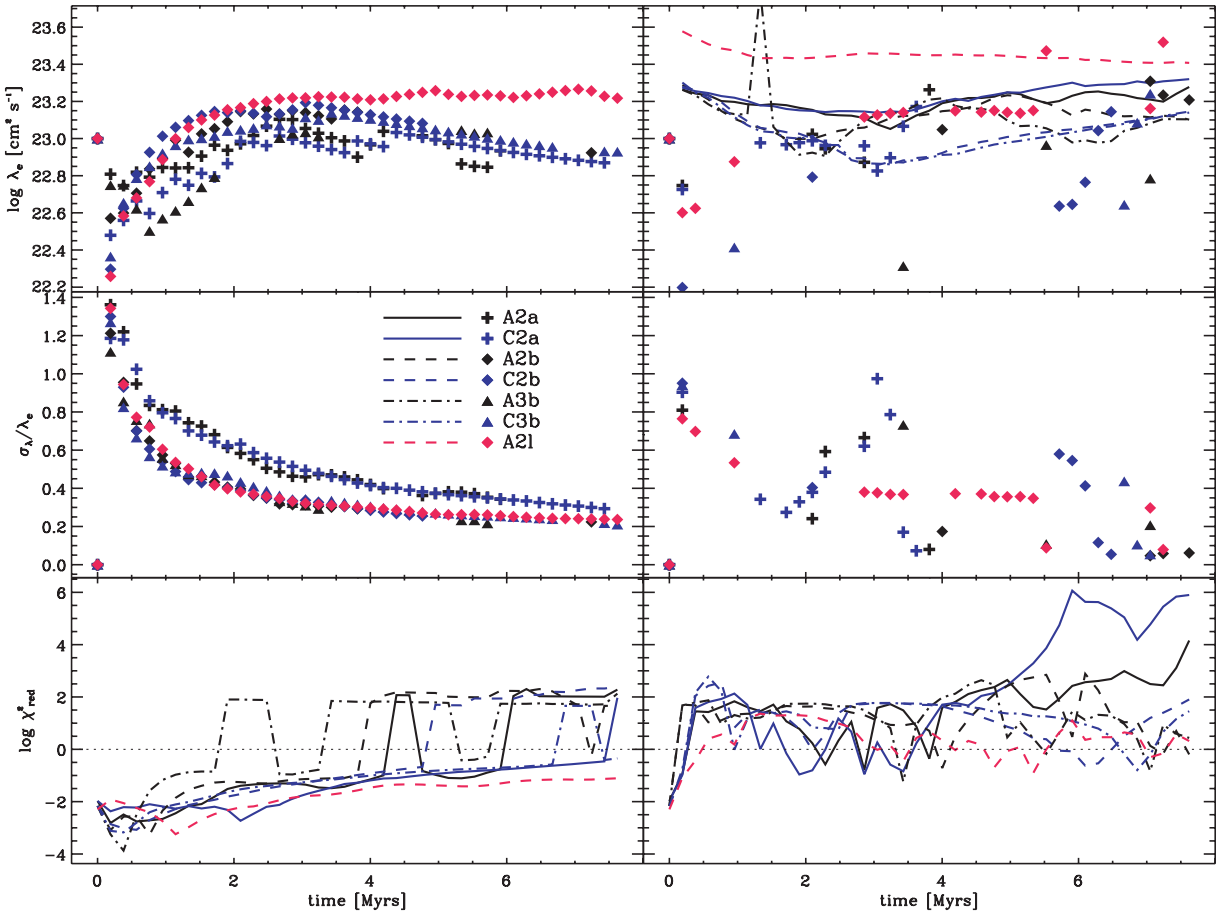

Figure 8. Diffusivities (top row), 1σ errors for profile fits (centre row), and reduced χ^2 for profile fits (bottom row), against time for all models. Left panels show results derived from filling factor profiles and right-hand panels show results derived from density profiles. Symbols in the top row panels denote diffusivities derived from profile fits (equation 8), lines in the top right-hand panel stand for λ_e derived from equation (9). Only fit diffusivities for $\chi^2_{red} < 2$ are shown.

later times, the overall decay of the turbulent rms velocity then leads to a decrease of the turbulent diffusivity.

The density profiles do not provide as nearly a complete picture as the filling factor profiles. Reliable fits are difficult to get because of shock waves travelling through the cloud. The few reliable fits clearly show that the diffusivities are not constant, but range within the same values as the ones derived from the filling factor profiles. As a crude check, the classically expected diffusivities

$$\lambda_e \equiv \langle R \rangle_M \, u_{rms} \tag{9}$$

are shown in the top right-hand panel of Fig. 8 in lines. Initially, they decrease slightly, mirroring the decay of u_{rms}, while the growing cloud radius compensates for the decaying velocity at later times. The values are within a factor of 2 at most times with the diffusivities derived from the profile fits. A $\lambda_e = 3 \times 10^{23}$ cm^2 s^{-1} would correspond to turbulent transport at 1 km s^{-1} over 1 pc.

Clearly, the diffusivities are not constant, which agrees with the findings of de Avillez & Mac Low (2002, 2003) and Klessen & Lin (2003). In a fully turbulent medium – whose energy scale distribution follows at least qualitatively a turbulent spectrum – the scale separation between turbulence and quantity to be diffused does not exist.

3.5 Cloud brightness

Turbulence considerably changes the density profiles of our model cloud, and reduces the optical depth at the centre of the cloud. Does turbulent transport (Section 3.4) and the exchange of warm diffuse and cold dense material (Section 3.3) carve tunnels and holes in the cloud through which radiation can enter? For an answer, we have to determine the radiation field within the cloud. Bethell et al. (2004) discussed this question with the help of a spherical cloud inscribed in a periodic box of evolved self-gravitating magnetohydrodynamic turbulence (Heitsch, Mac Low & Klessen 2001a; Heitsch et al. 2001b). This allowed them to study the radiation field inside an evolved structured cloud. Here, we are interested in the time-scales on which the radiation field changes.

To get a measure of the brightness inside the cloud, we determine the intensity of the radiation field at each point inside the cloud (see Bethell et al. 2004). Fig. 9 shows a scatter plot of the intensities inside the volume occupied by the original cloud against radius, for the four times indicated.

The brightness is calculated for each point by measuring the incident radiation for a given number of rays and averaging over the resulting sky. The ray number is determined such that at the outer surface of the cloud each resolution element is hit by one ray. Note

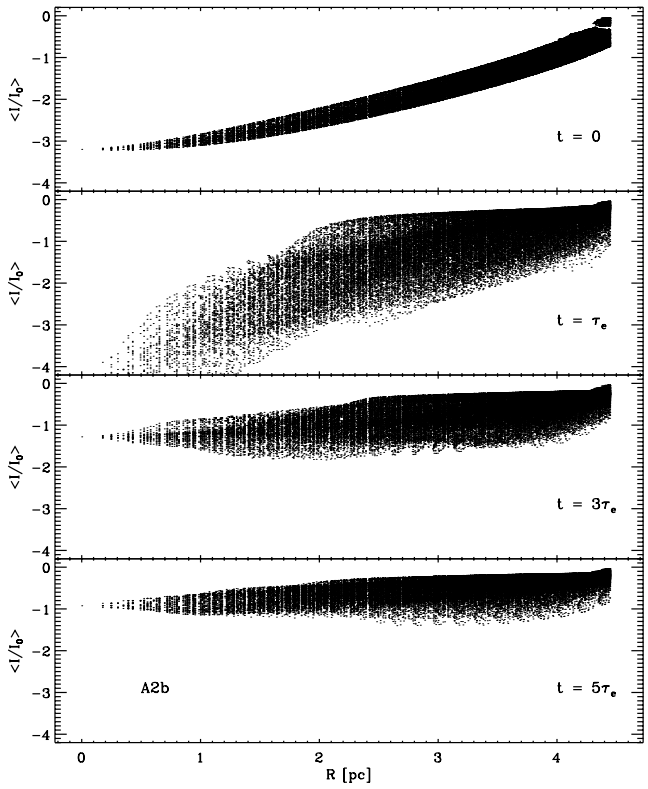

Figure 9. Scatter plots of relative brightness within cloud A2b, against radius, and for times as indicated in panels.

that while we plot only points up to the original radius of the cloud, the radiative transfer includes the whole domain, that is, we do not lose 'dense' material outside $R = 4.4$ pc which could shadow the inner parts. For extinction, we consider an effective extinction coefficient. Actual scattering is not included. In that sense our brightness estimates are lower limits.

The radially binned intensities resulting from plots like Fig. 9 for models A2b, C2b and A2l are shown in Fig. 10. Thick lines denote spherical volume averages at constant R, and thin lines spherical mass averages. Without self-gravity, the density contrasts in the cold material are small, so that volume and mass averages do not differ widely. Clearly, Fig. 10 mirrors the effect observed in Fig. 9: the cloud gets 'bright' within a few dynamical times, that is, the turbulence opens holes. Even for the larger cloud (A2l), the relative intensity does not drop below 10^{-3} anywhere in the cloud.

At late times, even the innermost regions receive more than a tenth of the incident radiation (models A2a/b, C2a/b, Fig. 11): turbulence (indirectly) lights up the cloud. The intensity at the centre of the cloud increases by at least two orders of magnitude. The central intensity for the models at lower resolution (thin lines, A2a and C2a) grows more smoothly than the intensity at higher resolution, and it reaches a slightly higher value at the end of the simulation. These are both resolution effects: the larger scatter comes from a more structured velocity field, and the larger central intensity is a consequence of fewer available grid cells along the line of sight. Still, for model A2l – with its initial cloud radius twice the size of those in models A2a/b – the central intensity increases by four orders of magnitude (compared to two for models A2a/b and C2a/b). Thus, we do not expect higher resolution to lead to progressively smaller central intensities.

The central intensities discussed so far are derived from averaging the incoming radiation over the whole 'sky' as seen from the cloud centre. If the turbulence digs tunnels in the cloud through which the irradiation can enter deep into the cloud, then this should be mirrored in the minimum (and maximum) optical depth at the centre of the cloud (Fig. 12). The extrema of the optical depths were taken over the whole sky as seen at the centre of the cloud. The mean optical depth corresponds to the centre intensities discussed above (note however that in order to derive the centre intensities, the *intensities* are averaged over the sky, not the optical depths).

As with the intensities (Fig. 11), the lower resolution runs lead to smaller average optical depths (Fig. 12, top right-hand panel). This is mostly a consequence of the lower minimum optical depths (top left-hand panel of same figure) and of the dominance of large-scale motions. Thus, the models run at 128^3 grid cells are not fully resolved, but should be used for demonstration purposes only. The strong spike for model C2b is a direct effect of the radiative cooling: compressed regions during the early turbulent evolution can reach much higher densities than possible for the adiabatic case. Although the minimum and maximum optical depth starts out at the same value, the maximum optical depth increases due to local compressions. Of course, the directions of minimum and maximum optical depth change with time. Models with different initial Mach number vary less than those with same Mach number but run at different resolution. Since the turbulence in our models is decaying, this is not surprising: most of the energy is lost in the early stages of the evolution.

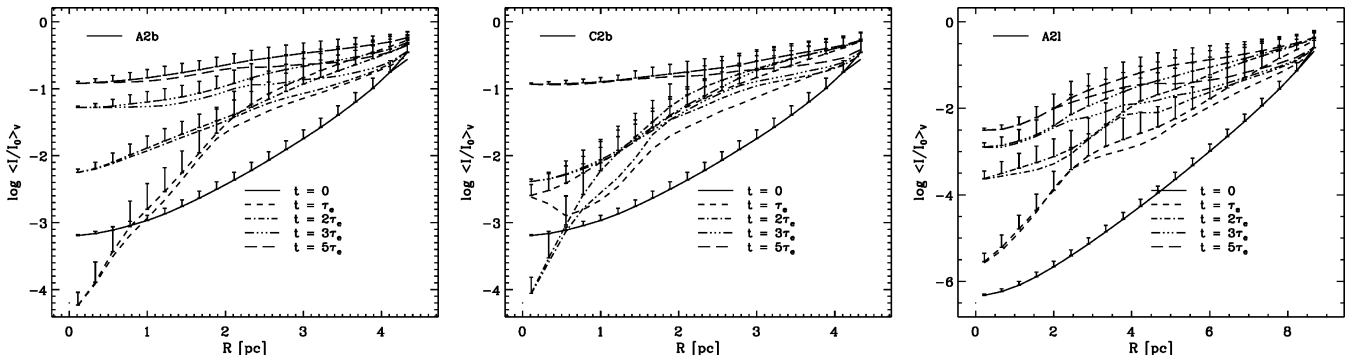

Figure 10. Radially binned intensities (see Section 3.5) for models A2b (left-hand panel), C2b (centre) and A2l (right-hand panel). Line styles denote the evolution time as indicated in the diagrams. Error bars represent errors on the mean. Thick lines are volume-averaged intensities, thin lines are mass-averaged intensities.

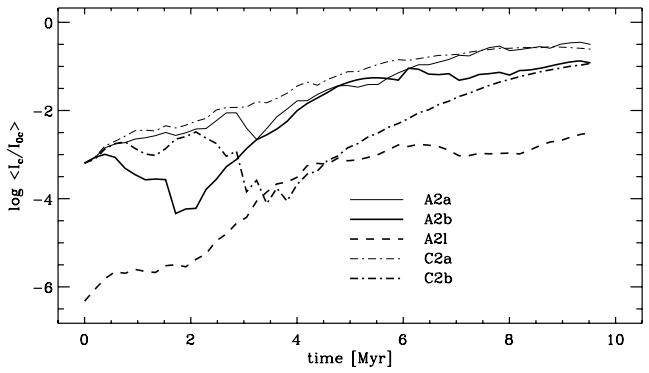

Figure 11. Central relative intensity against time for models A2a/b, C2a/b and A2l. Because of the larger cloud radius, model A2l stays at lower intensities.

Summarizing Fig. 12, the minimum optical depths drop by a factor of 4–8 (depending on the model), while the maximum optical depths increase by a factor of 2. Thus, while most of the brightening of the cloud stems from turbulent transport of dense material (see Section 3.2 and 3.3), compression and corresponding evacuation contributes as well. Finally, the average optical depths drop by a factor of 4 or more.

4 SUMMARY

Motivated by the highly dynamical nature of MCs and the question of how long a cold cloud can survive as a well-defined entity in a turbulent environment, we investigated the evolution of a cold cloud in a warm, turbulent medium, assessing the efficiency of the mixing by measuring the brightness inside the cloud. We showed that the properties of the initially solid cloud change thoroughly within a few dynamical time-scales.

While the column density maps can mislead, the brightness distribution inside the cloud clearly demonstrates that within a few dynamical times, the cloud becomes completely porous. Specifically, the cloud radius doubles within 5 dynamical times, while the filling factor of the cold gas drops to less than 50 per cent at the original cloud radius within one dynamical time. Cold material is bodily transported and exchanged with warm material (Figs 2 and 5). The turbulent diffusivity λ_e (equations 8, 9 and Fig. 8) is consistent with a fiducial number of $\lambda_e \approx 10^{23}$ cm^2 s^{-1}, corresponding to turbulent velocities and length-scales of approximately 1 km s^{-1} and 1 pc. The diffusivities are not constant with time.

The brightness estimates are lower limits, since we do not include scattering in the radiative transfer. Gravity might change the results by leading to additional fragmentation and thus to a growing discrepancy between volume- and mass-weighted intensity (Bethell et al. 2004). However, volume-wise, the cloud would get even brighter this way due to the smaller filling factor of the dense gas. The effects of H_2 (re-)formation remain to be discussed in subsequent models. If the turbulence were continually driven, we would expect an even faster dispersal. In that sense also, the presented time-scales are only upper limits.

The high radiation field within the cloud could strongly affect the chemistry and the dynamical state of the cloud (de Boisanger & Chièze 1991), leading to additional heating, H_2 destruction, and thus faster cloud disruption.

ACKNOWLEDGMENTS

We thank the referee for a critical, very detailed and constructive report. The idea for the present study arose during the IAU Symposium 227, 'Massive Star Birth: A Crossroads of Astrophysics'. We enjoyed discussions with C. F. McKee about MC lifetimes and turbulent dispersal, with K. Menten about small-scale structure in MCs and with E. Zweibel about turbulent transport. Computations were performed at the NCSA (AST040026), and on the SGI-Altix at the USM, built and maintained by M. Wetzstein and R. Gabler. FH enjoyed the hospitality of CRAL both at the ENS Lyon and the Observatoire de Lyon during several visits.

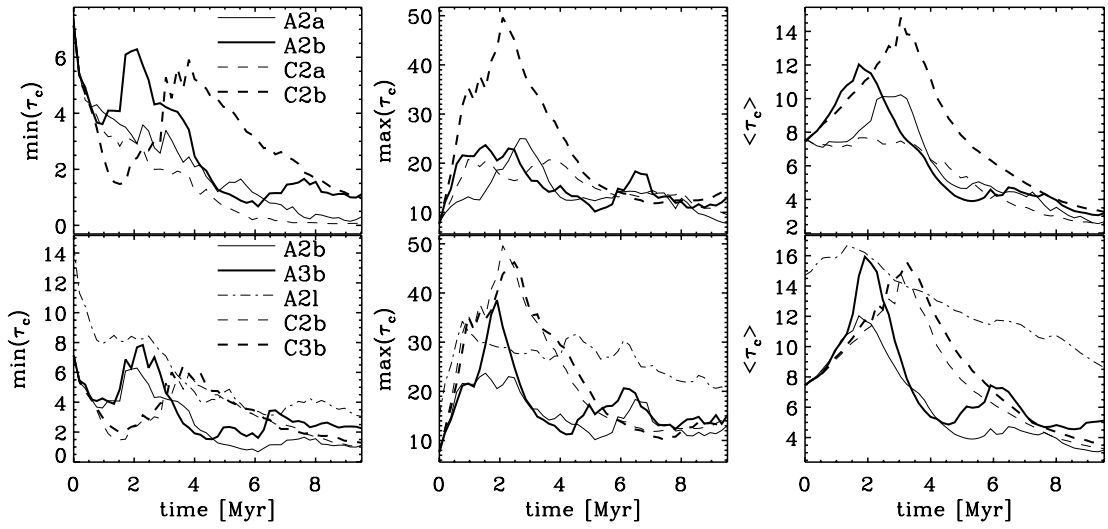

Figure 12. Optical depth at the centre of the cloud against time. Left-hand column: minimum optical depth. Centre: maximum optical depth. Right-hand column: average optical depth. Top row: models at resolution 128^3 (thin lines) and 256^3 (thick lines). Bottom row: parameter study. Thin lines denote models with an initial rms velocity of Mach 2, while thick lines stand for those with Mach 3.

REFERENCES

Balbus S. A., McKee C. F., 1982, ApJ, 252, 529
Ballesteros-Paredes J., 2006, MNRAS, 372, 443
Ballesteros-Paredes J., Hartmann L., Vázquez-Semadeni E., 1999, ApJ, 527, 285
Bethell T. J., Zweibel E. G., Heitsch F., Mathis J. S., 2004, ApJ, 610, 801
Bethell T. H., Zweibel E. G., Li P. S. 2006, ApJ, submitted
Cowie L. L., McKee C. F., 1977, ApJ, 211, 135
Cox D. P., Smith B. W., 1974, ApJ, 189, L105
de Avillez M. A., 2000, MNRAS, 315, 479
de Avillez M. A., Berry D. L., 2001, MNRAS, 328, 708
de Avillez M. A., Mac Low M.-M., 2002, ApJ, 581, 1047
de Avillez M. A., Mac Low M.-M., 2003, Rev. Mex. Astron. Astrofis. Ser. Con., 15, 290
de Boisanger C., Chièze J. P., 1991, A&A, 241, 581
Elmegreen B. G., 1993, ApJ, 419, L29
Elmegreen B. G., 2000, ApJ, 530, 277
Elmegreen B. G., Scalo J., 2004, ARAA, 42, 211
Falgarone E., Philips T. G., 1990, ApJ, 359, 344
Fox A. J., Savage B. D., Wakker B. P., Richter P., Sembach K. R., Tripp T. M., 2004, ApJ, 602, 738
Hartmann L., 2003, ApJ, 585, 398
Hartmann L., Ballesteros-Paredes J., Bergin E. A., 2001, ApJ, 562, 852
Heitsch F., Mac Low M.-M., Klessen R. S., 2001a, ApJ, 547, 280
Heitsch F., Zweibel E. G., Mac Low M.-M., Li P., Norman M. L., 2001b, ApJ, 561, 800
Heitsch F., Zweibel E. G., Slyz A. D., Devriendt J. E. G., 2004, ApJ, 603, 165
Heitsch F., Burkert A., Hartmann L., Slyz A. D., Devriendt J. E. G., 2005, ApJ, 633, L113
Heitsch F., Slyz A. D., Devriendt J. E. G., Hartmann L., Burkert A., 2006, ApJ, 648, 1052
Hennebelle P., Inutsuka S., 2006, ApJ, 647, 404
Klessen R. S., Lin D. N., 2003, Phys. Rev. E, 67, 046311
Landau L. D., Lifshitz E. M., 1966, Lehrbuch der theoretischen Physik VI. Hydrodyamik. Akademie-Verlag, Berlin
Lazarian A., 2006, ApJ, 645, L25
Mac Low M.-M., 2004, Ap&SS, 289, 323
Mac Low M.-M., Klessen R. S., 2004, Rev. Mod. Phys., 76, 125
Mac Low M.-M., Klessen R. S., Burkert A., Smith M. D., 1998, Phys. Rev. Lett., 80, 2754
McKee C. F., Cowie L. L., 1977, ApJ, 215, 213
McKee C. F., Ostriker J. P., 1977, ApJ, 218, 148
Moffatt H. K., 1978, Magnetic Field Generation in Electrically Conducting Fluids. Cambridge Univ. Press, Cambridge
Murray S. D., White S. D. M., Blondin J. M., Lin D. N. C., 1993, ApJ, 407, 588
Nulsen P. E. J., 1982, MNRAS, 198, 1007
Prendergast K. H., Xu K., 1993, J. Comp. Phys., 109, 53
Press W. H., Teukolsky S. A., Vetterling W. T., Flannery B. P., 1992, Numerical Recipes in C, 2nd edn. Cambridge Univ. Press, Cambridge
Pringle J. E., Allen R. J., Lubow S. H., 2001, MNRAS, 327, 663
Rosen A., Bregman J. N., 1995, ApJ, 413, 137
Schatzman E., 1977, A&A, 56, 211
Spitzer L., 1978, Physical Processes in the Interstellar Medium. Wiley, New York
Slyz A. D., Prendergast K. H., 1999, A&AS, 139, 199
Slyz A. D., Devriendt J. E. G., Bryan G., Silk J., 2005, MNRAS, 356, 737
Slyz A. D., Devriendt J. E. G., Bryan G., Heitsch F., Silk J. 2006, MNRAS, submitted
Vázquez-Semadeni E., Gazol A., Scalo J., 2000, ApJ, 540, 271
Vázquez-Semadeni E., Ryu D., Passot T., González R. F., Gazol A., 2006, ApJ, 643, 245
Vietri M., Ferrara A., Miniati F., 1997, ApJ, 483, 262
Williams J. P., Blitz L., McKee C. F., 2000, Protostars and Planets, Vol. IV. Univ. Arizona Press, Tucson AZ, p. 97
Wolfire M. G., Hollenbach D., McKee C. F., Tielens A. G. G. M., Bakes E. L. O., 1995, ApJ, 443, 152

This paper has been typeset from a TEX/LATEX file prepared by the author.